Three-dimensional chemical imaging of skin using stimulated Raman scattering microscopy

Dane M. Drutis
Thomas M. Hancewicz
Eugene Pashkovski
Lin Feng
Dawn Mihalov
Gary Holtom
Kavssery P. Ananthapadmanabhan
X. Sunney Xie
Manoj Misra

Three-dimensional chemical imaging of skin using stimulated Raman scattering microscopy

Dane M. Drutis,a,* Thomas M. Hancewicz,a Eugene Pashkovski,a,c Lin Feng,a Dawn Mihalov,a Gary Holtom,b Kavssery P. Ananthapadmanabhan,a X. Sunney Xie,b and Manoj Misraa
aUnilever Research and Development, Trumbull, Connecticut 06611
bHarvard University, Department of Chemistry and Chemical Biology, Cambridge, Massachusetts 02138
cThe Lubrizol Corporation, Wickliffe, Ohio 44092

Abstract. Stimulated Raman scattering (SRS) microscopy is used to generate structural and chemical three-dimensional images of native skin. We employed SRS microscopy to investigate the microanatomical features of skin and penetration of topically applied materials. Image depth stacks are collected at distinct wavelengths corresponding to vibrational modes of proteins, lipids, and water in the skin. We observed that corneocytes in stratum corneum are grouped together in clusters, 100 to 250 μm in diameter, separated by 10- to 25-μm-wide microanatomical skin-folds called canyons. These canyons occasionally extend down to depths comparable to that of the dermal–epidermal junction below the flat surface regions in porcine and human skin. SRS imaging shows the distribution of chemical species within cell clusters and canyons. Water is predominately located within the cell clusters, and its concentration rapidly increases at the transition from stratum corneum to viable epidermis. Canyons do not contain detectable levels of water and are rich in lipid material. Oleic acid-d$_{34}$ applied to the skin surface lines the canyons down to a depth of 50 μm below the surface of the skin. This observation could have implications on the evaluation of penetration profiles of bioactive materials measured using traditional methods, such as tape-stripping. © *The Authors. Published by SPIE under a Creative Commons Attribution 3.0 Unported License. Distribution or reproduction of this work in whole or in part requires full attribution of the original publication, including its DOI.* [DOI: 10.1117/1.JBO.19.11.111604]

1 Introduction

It is challenging to simultaneously obtain both structural and chemical information from intact skin tissue. Structural information is typically visualized by employing imaging techniques that detect reflected light, such as confocal laser scanning microscopy,[1–3] multiphoton fluorescence microscopy,[4] and optical coherence tomography.[5] Imaging by the techniques listed above typically does not provide specific information about chemical composition. A select number of autofluorescent species in skin tissue can be investigated without tissue preparation.[6] Exogenous fluorescent probes can be added, which provide indirect information about the skin chemistry.[7,8] With these two approaches, fluorescence imaging can provide chemical information for selected applications. Infrared and Raman spectroscopic imaging techniques give an abundance of chemical information from a multidimensional spectral data set,[9,10] but visualizing spatial distributions can require extensive data processing.[11,12]

Stimulated Raman scattering (SRS) microscopy is a label-free methodology for acquiring three-dimensional (3-D) structural information with a high degree of molecular specificity in real time.[13–15] Skin tissue contains multiple components that produce strong Raman responses in the high wavenumber region of the vibrational spectrum, including proteins, lipids, and water.[16] In the two-laser SRS system, the wavelengths are tuned to generate signal at frequencies corresponding to the

chemical components within the tissue. The nonlinear coherent excitation enhances the signal over conventional Raman spectroscopy. Rapid scanning of the lasers in the focal plane generates chemical images with submicron resolution at video rate. Step-wise movement of the focal plane creates an image stack for visualization of the 3-D structure of the skin. Image contrast is superior compared to coherent anti-Stokes Raman spectroscopy (CARS) due to the lack of background interference from autofluorescence or nonresonant signals.[13] An additional advantage over CARS is the nearly linear dependence of the SRS signal with concentration. This allows direct interpretation of the SRS vibrational spectrum and obviates the need for post-acquisition processing to visualize the chemical distribution.

The architecture of porcine epidermis has been visualized using two-photon confocal microscopy.[17] Porcine skin has been shown to have morphological and functional similarities to human skin.[18,19] The top layer of the skin, the stratum corneum, is composed of layers of cells called corneocytes. The corneocytes are observed to group together in clusters typically 100 to 250 μm across the surface. The cell clusters are separated from one another by microanatomical structures, termed canyons, which are invaginations or microfolds of stratum corneum cell layers. These SC canyons often reach the viable cells of the epidermis and may potentially provide delivery pathways for topically applied material.

SRS imaging is utilized in this work to probe the chemical nature of skin cluster and canyon microstructure by visualizing the distributions of proteins, lipids, and water throughout the cell cluster and canyon regions. This powerful spectroscopic technique provides the unique ability to obtain detailed 3-D

*Address all correspondence to: Dane M. Drutis, E-mail: dane.drutis@unilever.com

chemical images of the microscopic features of the layers of the skin. Image stacks were collected at three vibrational frequencies that approximately correspond to the Raman shifts of the three predominant skin chemical classes (Table 1). The spectroscopic information inherent in SRS imaging allows display of the spatial distribution of water across and through the skin layers, and identifies lipid-rich regions separating the water-rich cell clusters. The explicit chemical nature of the SRS signal also provides the opportunity to track the spreading of topically applied materials in native skin in real time without disruption. We investigate the diffusion of oleic acid, often used as a skin penetration enhancer.[20] Applying a fully deuterated molecule allows selection of a unique wavelength for imaging this material. Overlaying the oleic acid and skin images shows how the material can reach deeper layers.

2 Methods and Materials

2.1 Materials

Back and belly skin from Yucatan white, hairless pigs was received from Sinclair Bioresources (Auxvasse, Missouri). All tissues were harvested only as waste byproducts from animals aged three to six months. Tissues were only rinsed with water prior to shipment and were not frozen. A Padgett Electric Dermatome (Plainsboro, New Jersey) was used to isolate the top 500 μm of the skin. Pieces of the dermatomed skin, $\sim$1 cm^2, were placed between a glass microscope slide and No. 1.5 glass cover slip (VWR, Radnor, Pennsylvania) for SRS transmission microscopy. Oleic acid-d_{34} (Sigma-Aldrich, St. Louis, Missouri) was applied directly to the skin surface using a positive displacement pipette (Gilson, Middleton, Wisconsin) to deliver 2 μL onto a 1-cm^2 treatment area.

2.2 SRS Microscopic Imaging

The details of SRS have been previously described.[13,21] The skin sample is mounted on the stage of a modified upright laser scanning microscope (BX81, Olympus, Pittsburgh, Pennsylvania) configured for transmission illumination. Two overlapping laser beams are focused on the sample with either a UPLSAPO20X 20$\times$ air objective or a UPLSAPO60XW 60 $\times$ 1.2-NA water immersion objective (Olympus). The 1064-nm Stokes beam source was an Nd:YVO_4 laser (picoTRAIN, High-Q, Watertown, Massachusetts). Part of the 1064-nm output is used to pump a tunable optical parametric oscillator (Levante Emerald,

Table 1 Wavelengths and Raman assignments for stimulated Raman scattering (SRS) imaging. The four wavelengths selected with the pump probe for this study and the corresponding Raman shifts, vibrational mode assignments, and the primary chemical species contributing to the SRS signal are shown.

Pump beam wavelength (nm)	Raman shift (cm^{-1})	Vibrational mode	Band assignment
781.3	3340	ν(OH)	Water
810.6	2950	ν(CH_3)	Protein and lipid
816.0	2850	ν(CH_2)	Lipid
869.3	2105	ν(CD)	d_{34}-oleic acid

APE-Berlin, Berlin, Germany). The pump beam was tuned to 816.0, 810.6, or 781.3 nm for skin imaging, corresponding to Raman shifts of ca. 2850, 2950, or 3340 cm^{-1}, respectively. The main contributors from skin at these vibrational frequencies can be assigned to vibrational modes from lipids, proteins, and water[22] (Table 1). The pump laser was tuned to 869.2 nm to image the ν(C-D) vibrational mode at 2105 cm^{-1} after topical application of oleic acid-d_{34}, ensuring that only the applied material would be visible in the SRS image stack. Image integration time was typically 4 to 8 μs/pixel. The beams were scanned in two dimensions with a pair of galvanometer mirrors (Olympus fluosview FV-300). The transmitted light was collected with a 1.4-NA oil condenser lens (Nikon, Melville, New York) and detected by a large-area photodiode (FDS1010, Thorlabs, Newton, New Jersey). Images were collected parallel to the skin surface. Image stacks were obtained through sample stage movements controlled by the microscope software, with a step size of 2 μm over depth ranges of 60 to 100 μm. An image stack at a single wavelength can be acquired in 30 to 60 s.
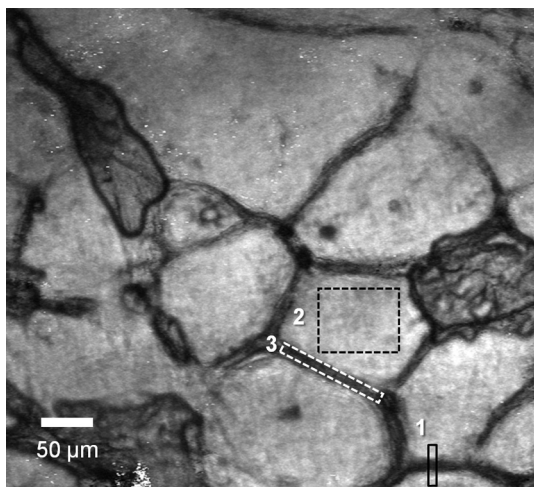
2.3 SRS Image Analysis

The three associated image stacks (lipid, protein, and water) were combined into a four-dimensional (4-D) array (X,Y,Z, wavelength) in MATLAB® (version 2009a, MathWorks, Natick, Massachusetts). The region of interest (ROI) (cell cluster and/or canyon) was designated on the water image using a rectangular area selection tool that records the pixel location values for all selected points. Depth profiles for each pixel location in the ROI are extracted from the 4-D array for each wavelength. The water profiles for clusters and canyons were computed using the method previously reported for *in vivo* confocal Raman spectroscopic measurements.[23] Each water profile was normalized against the corresponding protein depth profile with a calibration factor of 1. The SRS technique minimizes background response [typically <1% of the peak ν(CH_2) intensity[15]], but a small profile is present in the image response. The background signal is neither spectroscopic nor resonant in origin. The magnitude of this response will change slightly at different regions of the Raman spectrum, but since the wavelengths we are using are very near to each other, the ratio method used for analysis will cancel out background effects. Additionally, the method proposed by Caspers et al. is, at best, an approximation due to their use of overlapping spectral bands for protein and water.[23] A pure response is, therefore, never achieved, so any calculation for the constant (R) can only ever yield an approximate value because it is dependent on the calculated values for water and protein. We used the same equation but replaced R = 2 with the arbitrary value of R = 1. This maintains the same profile shape but changes the absolute scale. Depth profile plots are presented as relative water content. The water content approximation, therefore, was modeled after the Caspers method as (percent relative water content) = $\{(W/P)/[(W/P) + R]\} * 100$, where W and P are the intensities from the water and protein images, respectively, and R = 1. W and P represent single-wavelength intensities from the SRS images, whereas the confocal *in vivo* Raman spectroscopic method employs integrated wavelength ranges. The water content values reported here are averaged over all pixels in the ROI. Lipid content values are also generated by a similar protocol, with the lipid intensity L replacing water intensity W in the above equation.

Cross-sections calculated across canyon regions were generated by selecting a rectangular ROI of the water image stack and averaging across the planes to form a single water depth profile. The resulting images are displayed using a relative normalized scale from 0 to 255, corresponding to the gray-scale range of the original images. The red false color indicates high water content and the blue false color represents low water content. The overlaid 3-D surface contour images of oleic acid-d_{34} and the skin protein microstructure were generated in Amira (version 5.4, Visage Imaging, San Diego, California). False colors were selected to maximize contrast between the two images in the 3-D rendering.

3 Results

3.1 Skin Microstructure

An example of the cluster and canyon structure of porcine skin is shown in an SRS water (3340 cm^{-1}) image collected near the skin surface at 20× magnification (Fig. 1). In SRS images, the intensity of each pixel corresponds to the amount of the chemical component(s) with a Raman signal at that vibrational frequency. In this data, there is some contribution in each of the single-wavelength images to components other than the labeled chemical component. Every effort was made to minimize overlap with the other component images so as to maximize image purity. The idea here is not to present absolute quantitation of the component content from the images, but rather to show that differences in chemical information can be obtained in a relatively straightforward manner. The water (3340 cm^{-1}) image shows a clear distinction between high-intensity water-rich cellular regions (cell clusters), such as region 2 in Fig. 1, and low-intensity water-deficient canyons separating the clusters (region 3). Multiple cell clusters and canyons are observed at this lower magnification. More detailed examination of the changes in skin microstructure as a function of depth can be accomplished by collecting multiple image stacks at 60× magnification. The unique and varying architecture of the epidermal layers is represented in SRS images selected from different depths in three
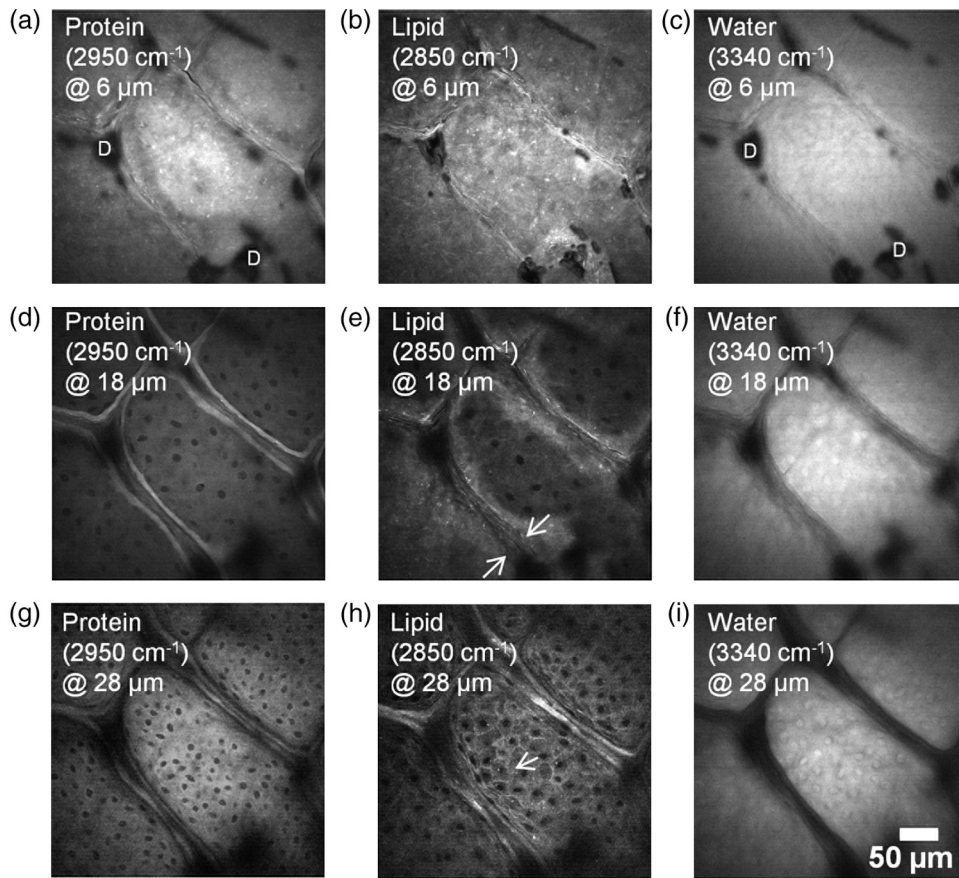
image stacks acquired at the higher 60× magnification (Fig. 2). The three columns show images taken at the frequencies corresponding to protein (2950 cm^{-1}), lipid (2850 cm^{-1}), and water (3340 cm^{-1}), while the three rows portray depths of 6, 18, and 28 μm below the surface. Near the surface of the skin, the corneocytes aggregate into clusters ranging from 100 to 250 μm wide [Figs. 2(a) to 2(c)]. Lipid, protein, and water content appear to be distributed across the visible areas, as evidenced by the approximately uniform SRS intensities for each of the three frequencies. The dark spots in these images (marked "D" in the first row of images) are optical shadows from air pockets between the skin surface and coverslip. The corneocyte clusters are separated by invaginations 10 to 25 μm wide, features previously designated as canyons.[17]

The transition from the stratum corneum into the viable epidermis is discernible in images collected 18 μm below the surface [Figs. 2(d) to 2(f)]. At this depth, the distinct boundaries between the clusters are visible, such as between the arrows in Fig. 2(e). The average canyon width in these images is 21.2 ± 4.4 μm. The signal intensity in the protein and lipid images is highest along the canyon walls, as evidenced by the bright lines outlining the canyons [Figs. 2(d) and 2(e)]. Fine lines are visible between the canyons, as can be seen between the arrows in the lipid (2850 cm^{-1}) image [Fig. 2(e)]. These are the edges of stratum corneum corneocytes following the contours of the canyon, as has previously been proposed.[17] The water signal is significantly weaker in the canyons than in the cluster regions. In the cluster regions, nuclei are visible as dark ovals in the protein and lipid images [Figs. 2(d) and 2(e)], and as bright ovals in the water image [Fig. 2(f)]. Around this depth, the distinctive polygonal shape of the cells is revealed as the lipid-rich cell wall membranes appear in the lipid (2850 cm^{-1}) image [Fig. 2(e)]. The chemical specificity of SRS imaging allows these cell walls to be visualized, whereas they are often missed in other optical techniques, such as autofluorescence.[13,17]

Looking deeper into the epidermis at 28 μm below the surface, the canyons become progressively narrower [Figs. 2(g) to 2(i)]. The water (3340 cm^{-1}) image is dark between the cell clusters, indicating any water that may be present in the canyons is below the limit of detection. The cell walls are brightly illuminated in the lipid (2850 cm^{-1}), showing the cell shape becoming rounder [Fig. 2(h)]. The density of visible nuclei has increased in this layer.

3.2 Depth Profiles

Measured SRS signals are proportional to molecular concentration, providing a distinct advantage over nonlinear techniques, such as CARS.[8] This linear dependence is a requirement for quantitative examination of the spatial distribution of chemical species within skin substructures. The relative water content spanning one intercluster canyon was averaged through all images of the water (3340 cm^{-1}) depth stack at each pixel location from the 65 × 15 pixel region designated as region 1 in the 20× water image (Fig. 1). The average water content values are plotted as a false color map, distinctly showing the boundary between the water-rich cells (displayed in red) and the water-free canyon (in blue) (Fig. 3). The red false color indicates high water content and the blue false color represents low water content. This visual representation can be used to measure the distance between the two clusters. For this example, the widest gap—the spacing between the two bright red regions—is

Fig. 1 Stimulated Raman scattering (SRS) images show the organization of corneocytes into clusters and canyons. A single SRS image acquired at 3340 cm^{-1} at 20× magnification from porcine skin. Pixel intensity corresponds to water content, with cell clusters appearing bright, separated by the dark regions defining canyons. Multiple cell clusters can be seen at this lower magnification. Scale bar = 50 μm.

Fig. 2 Changes in chemical distribution are visible by collecting depth stacks at multiple wavelengths. SRS images were acquired at 60× magnification from pig skin. The rows correspond to focal planes 6 μm [(a) to (c)], 18 μm [(d) to (f)], and 28 μm [(g) to (i)] below the skin surface. The columns from left to right represent protein, lipid, and water content, respectively, according to the band assignments given in Table 1. The dark spots labeled "D" in (a) and (c) are due to optical shadows from air pockets between the skin surface and coverslip. The arrows in (e) designate one canyon in the image. Fine lines can also be seen within the canyon. The arrow in (h) points to one of the visible cell membranes in the cluster. Scale bar = 50 μm.
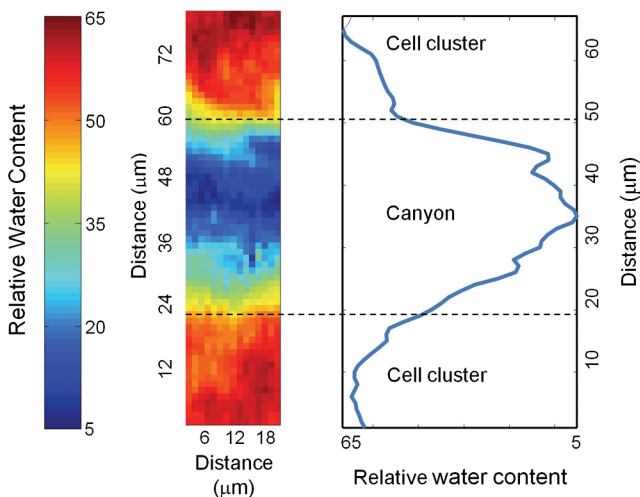
Fig. 3 Analysis of SRS water depth stack shows water resides exclusively within the cell clusters. The color map calculated from region 1 of the SRS water image in Fig. 1 indicates the relative water content at each pixel through the complete 60 μm of the depth stack. Red regions are high in water content and correspond to the location of the cells. The water profile on the right aggregates the calculated values across each row of pixels.

~30 pixels, corresponding to a width of ~37 μm. The water map gives an indication of the varying canyon width as a function of depth. The weaker water signals shown in yellow and green correspond to narrowing of the canyon at a depth of ~20 μm. The water content of each pixel is averaged through the entire stack. The pixels shown in yellow and light blue are located in areas that are open canyons near the surface, but viable cells deeper in the skin.
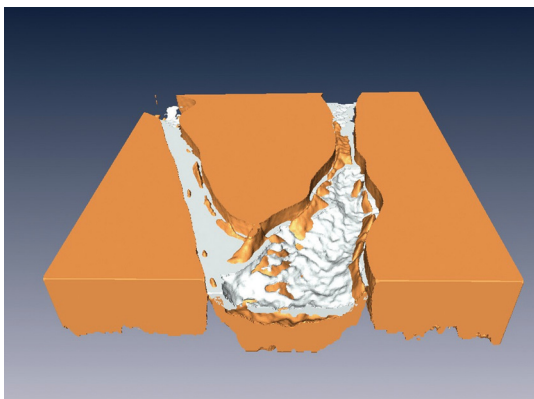
This technique provides detailed depth information about the hydration of skin and the distribution of water throughout the substructures. The mean water signal intensity was calculated throughout the image depth stack for the cluster and canyon features designated as regions 2 and 3 in Fig. 1. Water depth profiles are generated from the intensities in the protein (2950 cm^{-1}) and water (3340 cm^{-1}) images, as described above. These depth profiles further demonstrate that the water content of the skin resides predominantly within the cellular areas and not in the canyons [Fig. 4(a)]. The distribution of water within cell clusters, shown here as a function of depth, is in agreement with water profiles measured using *in vivo* confocal Raman spectroscopy in human skin.[10] In healthy skin, the water content is ~30% in the stratum corneum. There is a sharp rise in water content located at the boundary between the stratum corneum and viable cells, eventually reaching a plateau of 60 to 70%.
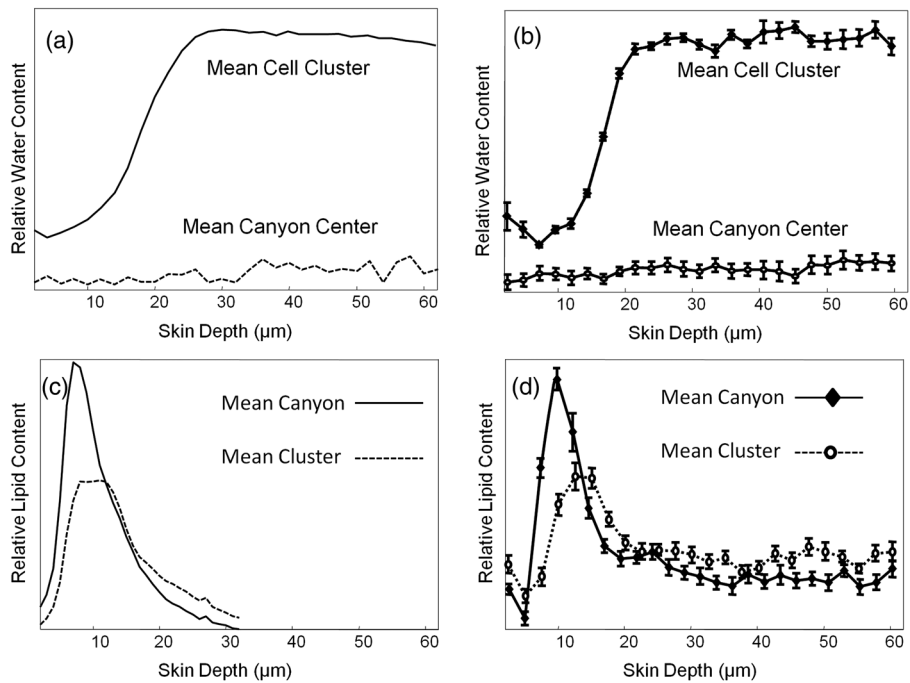
Fig. 4 Depth profiles show water distribution increasing in the lower layers of the skin [(a) and (b)], while lipid material resides in the canyon near the skin surface [(c) and (d)]. The water profiles shown in (a) were normalized against protein content and calculated for the cluster and canyons regions designated 2 and 3 in Fig. 1, while (b) shows the mean plot of the analysis of three different images. The sharp increase in water content in the cell clusters at 20 μm corresponds to the transition from the stratum corneum to the viable cells of epidermis. The lipid profiles shown in (c) were also normalized against protein content and calculated for the cluster and canyon regions designated 2 and 3 in Fig. 1, while (d) shows the mean plots of the analysis of three different images. The high levels of lipid signal from the canyon region between 5 and 10 μm below the skin surface confirms the presence of lipid along the canyons. The error bars in (b) and (d) represent 95% confidence interval of the mean at each point.

We observed the same sigmoidal profile of water as a function of depth in SRS image data [Fig. 4(b)] as seen in single-point *in vivo* confocal Raman microspectroscopy data.

This same analytical approach can be employed to generate lipid depth profiles. Using the same ROI 2 and 3 from Fig. 1, evaluation of the lipid (2850 cm^{-1}) image stack shows that there

is a significant accumulation of lipid material near the top of the canyon [Fig. 4(c)]. These canyon lipids are in a discrete volume, as evidenced by the sharp maximum in the lipid profile, in contrast to the relatively even distribution in the cell clusters. Lipid levels in all areas start to decline 15 μm below the skin surface [Fig. 4(d)]. It is important to consider that the signal at 2850 cm^{-1} is not exclusively from skin lipids and may include some contribution from protein as well.

3.3 Active Penetration

Canyons can potentially play a role in the delivery of materials into the viable skin cells depending upon the compactness, thickness, and ultrastructure of stratum corneum that forms the canyon walls. We are beginning to explore possible penetration pathways by evaluating the diffusion of oleic acid-d$_{34}$ topically applied to the porcine skin surface. Figure 5 shows a 3-D space model rendered from two SRS image stacks collected after application of oleic acid. The canyon and cluster structure of the skin is colored orange in the 3-D image obtained from the protein signal in the SRS stack. A separate oleic acid image stack was obtained for the C-D stretching mode at ca. 2105 cm^{-1} 25 min after treatment. The oleic acid surface contour map is superimposed in white against the canyon structure, showing the deuterated material residing in the canyon and coating the canyon walls. This example shows penetration of materials deep into the canyons in a short period of time.

Fig. 5 Three-dimensional (3-D) surface plot shows oleic acid-d$_{34}$ filling the canyons. The shape of a canyon structure is visualized by rendering the protein SRS image stack as a 3-D surface plot, shown in orange. The ν(CD) stretching mode rendering is overlaid in white onto the protein image, showing the d$_{34}$-oleic acid remains within the canyon 25 min after application. The oleic acid film sitting on the surface of the clusters was excluded from the rendering to improve the visibility of the canyon material. The 3-D volume represented in these images is ca. $630 \times 630 \times 50$ μm^3.

4   Conclusions

The quantitative spectroscopic response of SRS enables extraction of relative component concentration profiles directly from the image depth stacks. This can be employed not only to understand the chemical composition of skin features, but also to follow delivery and penetration of actives in real time. SRS imaging provided an improved understanding of the skin architecture first observed with two-photon microscopy.[17] We have been able to build upon those classifications by identifying the chemical nature of canyons and cell clusters. Canyons are low in water content and occasionally contain lipidaceous material capping the top of the canyon close to the skin surface. The oleic acid example shows that the material can be located within skin substructures at different depths. Transdermal diffusion is typically measured by collecting all the materials passing through a thick (~500 μm) piece of skin in a Franz cell. Stratum corneum and epidermal penetration have typically been assessed by removing layers of skin by tape-stripping and conducting quantitative analysis of the individual tapes.[20,24] An apparent drawback of the layer-by-layer approach exposed here is that material sitting deep in the canyon might be considered "penetrated" active. In contrast, SRS shows that the oleic acid is primarily present in the canyons and has not entered into the cells in the cluster regions of the skin after 25 min of exposure. SRS microscopy, thus, provides the unique opportunity to investigate penetration pathways of actives at high spatial resolution by exploiting the intrinsic contrast of the active.

SRS microscopy provides a unique view of the chemical organization of the skin, rapidly and noninvasively assessing the layers of intact tissue. These experiments were conducted with *a priori* knowledge of the tissue, which enabled selection of distinct, representative wavelengths for imaging the key components of the skin chemical structure. When interpreting the images, one must remember that these spectroscopic bands are not unique for a single chemical species. For example, the $\nu(CH_3)$ wavelength assigned to protein does contain a small contribution from lipid content. Multivariate analysis is preferred over single-wavelength evaluation, as shown previously.[11,25,26] The speed of the hardware to perform rapid wavelength changes is a limiting factor toward implementation of multivariate analysis. Development of the instrumentation will progress toward fast multiwavelength spectroscopy when a large spectral window can be scanned, opening new areas of exploration. The expanded wavelength domain will enhance the ability to identify and distinguish components with similar chemical structures and overlapping spectroscopic signatures, such as distinct lipid components present within the skin.

Acknowledgments

References

1. M. Rajadhyaksha et al., "In vivo confocal scanning laser microscopy of human skin: melanin provides strong contrast," *J. Invest. Dermatol.* **104**(6), 946–952 (1995).
2. K. Sauermann et al., "Age related changes of human skin investigated with histometric measurement by confocal laser scanning microscopy in vivo," *Skin Res. Technol.* **8**(1), 52–56 (2002).
3. S. Neerken et al., "Characterization of age-related effects in human skin: a comparative study that applies confocal laser scanning microscopy and optical coherence tomography," *J. Biomed. Opt.* **9**(2), 274–281 (2004).
4. K. König, "Multiphoton microscopy in life sciences," *J. Microsc.* **200**(2), 83–104 (2000).
5. T. Gambichler and V. Jædicke, "Optical coherence tomography in dermatology: technical and clinical aspects," *Arch. Dermatol. Res.* **303**(7), 457–473 (2011).
6. C. L. Evans et al., "Chemical imaging of tissue in vivo with video-rate coherent anti-Stokes Raman scattering microscopy," *Proc. Natl. Acad. Sci. U. S. A.* **102**(46), 16807–16812 (2005).
7. C. L. Evans and X. S. Xie, "Coherent anti-Stokes Raman scattering microscopy: chemical imaging for biology and medicine," *Annu. Rev. Anal. Chem.* **1**, 883–909 (2008).
8. W. Min et al., "Coherent nonlinear optical imaging: beyond fluorescence microscopy," *Annu. Rev. Phys. Chem.* **62**, 507–530 (2011).
9. H. U. Gremlich and B. Yan, Eds., *Infrared and Raman Spectroscopy of Biological Materials*, Marcel Dekker Inc., New York (2001).
10. P. J. Caspers, G. W. Lucassen, and G. J. Puppels, "Combined in vivo confocal Raman spectroscopy and confocal microscopy of human skin," *Biophys. J.* **85**(1), 572–580 (2003).
11. J. J. Andrew and T. M. Hancewicz, "Rapid analysis of Raman image data using two-way multivariate curve resolution," *Appl. Spectrosc.* **52**(6), 790–796 (1998).
12. T. M. Hancewicz and J. H. Wang, "Discriminant image resolution: a novel multivariate image analysis method utilizing a spatial classification constraint in addition to bilinear nonnegativity," *Chemom. Intell. Lab. Syst.* **77**(1), 18–31 (2005).
13. C. W. Freudiger et al., "Label-free biomedical imaging with high sensitivity by stimulated Raman scattering microscopy," *Science* **322**(5909), 1857–1861 (2008).
14. B. G. Saar et al., "Video-rate molecular imaging in vivo with stimulated Raman scattering," *Science* **330**(6009), 1368–1370 (2010).
15. B. G. Saar et al., "Imaging drug delivery to skin with stimulated Raman scattering microscopy," *Mol. Pharmaceutics* **8**(3), 969–975 (2011).
16. L. Chrit et al., "In vivo chemical investigation of human skin using a confocal Raman fiber optic microprobe," *J. Biomed. Opt.* **10**(4), 044007 (2005).
17. D. C. Carrer, C. Vermehrenand, and L. A. Bagatolli, "Pig skin structure and transdermal delivery of liposomes: a two photon microscopy study," *J. Control. Release* **132**(1), 12–20 (2008).
18. G. A. Simon and H. I. Maibach, "The pig as an experimental animal model of percutaneous permeation in man: qualitative and quantitative observations—an overview," *Skin Pharmacol. Appl. Skin Physiol.* **13**(5), 229–234 (2000).
19. A. M. Barbero and H. F. Frasch, "Pig and guinea pig skin as surrogates for human in vitro penetration studies: a quantitative review," *Toxicol. Vitro* **23**(1), 1–13 (2009).
20. A. Naik et al., "Mechanism of oleic acid-induced skin penetration enhancement in vivo in humans," *J. Control. Release* **37**(3), 299–306 (1995).
21. M. B. J. Roeffaers et al., "Label-free imaging of biomolecules in food products using stimulated Raman microscopy," *J. Biomed Opt.* **16**(2), 021118 (2011).
22. B. W. Barry, H. G. M. Edwards, and A. C. Williams, "Fourier transform Raman and infrared vibrational study of human skin: assignment of spectral bands," *J. Raman Spectrosc.* **23**(11), 641–645 (1992).
23. P. J. Caspers et al., "In vivo confocal Raman microspectroscopy of the skin: noninvasive determination of molecular concentration profiles," *J. Invest. Dermatol.* **116**(3), 434–442 (2001).
24. A. Cappiello et al., "Application of liquid chromatography-direct-electron ionization-MS in an in vitro dermal absorption study: quantitative determination of trans-cinnamaldehyde," *Anal. Chem.* **83**(22), 8537–8542 (2011).
25. C. Xiao et al., "Uncertainties in depth determination and comparison of multivariate with univariate analysis in confocal Raman studies of a laminated polymer and skin," *Appl. Spectrosc.* **58**(4), 382–389 (2004).
26. T. M. Hancewicz et al., "Improved modeling of in vivo confocal Raman data using multivariate curve resolution (MCR) augmentation of ordinary least squares models," *Appl. Spectrosc.* **67**(12), 1463–1472 (2013).

Biographies of the authors are not available.